Tuning thermal transport in highly cross-linked polymers by bond-induced void engineering

Debashish Mukherji [1,*] and Manjesh Kumar Singh[2]
[1]*Quantum Matter Institute, University of British Columbia, Vancouver BC V6T 1Z4, Canada*
[2]*Department of Mechanical Engineering, Indian Institute of Technology Kanpur, Kanpur UP 208016, India*

(Received 17 December 2020; accepted 9 February 2021; published 22 February 2021)

Tuning the heat flow is fundamentally important for the design of advanced functional materials. Here polymers are of particular importance because they provide different pathways for the energy transfer. More specifically, the heat flow between the two covalently bonded monomers is over 100 times faster than between the two nonbonded monomers interacting via the van der Waals (vdW) forces. Therefore, the delicate balance between these two contributions often provides a guiding tool for the tunability in thermal transport coefficient κ of the polymeric materials. Traditionally most studies have investigated κ in the linear polymeric materials, the recent interests have also been directed towards the highly cross-linked polymers (HCP). In this work, using the generic molecular dynamics simulations, we investigate the factors effecting κ of HCP. We emphasize the importance of the cross-linking bond types and their influence on the network microstructure, with a goal of providing a guiding principle for the tunability in κ. While these simulation results are discussed in the context of the available experimental data, we also make predictions.

DOI: 10.1103/PhysRevMaterials.5.025602

I. INTRODUCTION

Polymers are an important class of high entropy materials that are extremely important for our everyday life [1,2], with possible applications for household items [3,4], electronic packaging [5], organic solar cells and light emitting diodes [6,7], thermoelectrics [8–10], and defense materials [11,12]. The standard architecture of a polymer chain consists of a string of covalently bonded monomers that exhibit interesting properties at different length, time, and energy scales [1,2]. Another class is when each monomer can form multiple bonds with its neighbors, commonly known as the highly cross-linked polymers (HCP). Because of the network connectivity, HCPs are lightweight, high performance materials that often exhibit extraordinary and unexpected mechanical behavior [11–14]. Here, one quantity that is intimately linked to the mechanical response of a materials is its thermal transport coefficient κ [15,16]. In this context, understanding the heat propagation in bulk polymers is highly challenging task because of their complex microstructure, which has tremendous potential in designing advanced functional materials with tunable properties [5,17,18].

Studying the heat flow in polymers is microscopically interesting because at the monomer level there are two distinct pathways for the energy transfer, i.e., between two covalently bonded monomers and nonbonded neighbors dictated by the van der Waals (vdW) contacts [19–22]. The strength of the vdW interaction is less than k_BT, while it is $80k_BT$ for the covalent bonds [2,23]. Here, k_B is the Boltzmann constant and $T = 300$ K. Owing to this stark contrast in the relative interaction strengths, the material stiffness also changes from about 5 GPa for the vdW interactions [17] to larger than 250 GPa for a covalent bond [24], and thus leads to a contrast $\kappa_{\text{covalent}}/\kappa_{\text{vdW}} > 100$ [20]. In the case of the hydrogen bonding between the nonbonded monomers, the strength of which is about $4k_BT$, $\kappa_{\text{H-Bond}}/\kappa_{\text{vdW}} \simeq 2-4$ [17,18], it also reduces $\kappa_{\text{covalent}}/\kappa_{\text{H-bond}}$. Therefore, the faster energy flow between two bonded neighbors will automatically infer that κ for a bulk polymeric material can be increased by increasing the bond density ρ_b, i.e., a higher value of ρ_b will be expected to significantly increase κ. Here, a prototypical system is the HCP where the physical properties are dominated by the three–dimensional network of bonds [11–14]. Moreover, the experiments have shown that this standard understanding does not always hold, instead κ with different cross-linking types exhibits rather anomalous behavior [25–27]. For example, most HCP can only show an improvement in κ by about 1.1–1.3 times in comparison to the standard linear polymeric materials, while κ is even lower for some HCPs than the linear chains [26].

Traditionally, most simulation studies on HCP are devoted in investigating the network structures and their mechanical properties. These include from the generic [13,14] to the multiscale [28,29], and to all-atom molecular dynamics simulations [12,30]. Recent investigations are also devoted to study the thermal transport of HCP [25,27]. In this context, while the all-atom simulations are useful for the quantitative comparisons with the experimental data, they also pose a significant challenge from the computational perspective. For example, due to the lack of the microstructural network details of the realistic systems,- curing is always a nontrivial task within the all-atom setups, restricting the accessibility to a wide range of macromolecular structures and often limited to the goodness of the force field parameters. Therefore, a generic model can provide a better alternative in giving the underlying physical

*debashish.mukherji@ubc.ca

mechanism, and also provides the necessary flexibility for the parameter tuning in these complex systems [13,14,27]. Motivated by these observations, the goal of this work is to investigate the effects of bonding on the network microstructure of HCP and κ, with an aim to propose a generic scheme that can serve as a guiding principle for future experimental studies.

The remainder of the paper is organized as follows: In Sec. II, we sketch our methodology. Results and discussions are presented in Sec. III, and the conclusions are drawn in Sec. IV.

II. MODEL AND METHOD

For this study we have chosen a set of neat HCP with different network functionality n, i.e., each monomer can form a maximum of n bonds. Here, we choose trifunctional (i.e., $n = 3$) and tetrafunctional (i.e., $n = 4$) HCP. We have also simulated a set of monodispersed linear polymer melts with a chain length $N_\ell = 50$. This specific choice of $N_\ell = 50$ is because this length gives a reasonable estimate of the single chain structure in a melt, while not approaching the entanglement effect that comes into play for $N_\ell > 70$ [31]. Furthermore, κ of a linear polymer melt does not depend on N_ℓ for $N_\ell > 10$, which is about 10 Kuhn lengths ℓ_k for a fully flexible generic chain [31]. We also wish to mention that N_ℓ usually influences κ for the chain oriented (stretched) systems. The detailed discussion on this aspect is beyond the scope of our present study. In all these systems, the total number of monomers in a simulation box is taken as $N = 2.56 \times 10^5$.

A. Interaction potentials

We employ a generic molecular dynamics simulation approach. All nonbonded interactions are modelled using a 6–12 Lennard-Jones (LJ) potential,

$$u_{\text{non-bonded}}(r) = 4\epsilon\left[\left(\frac{\sigma}{r}\right)^{12} - \left(\frac{\sigma}{r}\right)^{6} + \left(\frac{\sigma}{r_c}\right)^{12} - \left(\frac{\sigma}{r_c}\right)^{6}\right] \quad \text{for } r < r_c, \tag{1}$$

with an interaction cutoff distance $r_c = 2.5\sigma$. Here, ϵ and σ are the LJ energy and LJ length, respectively. This leads to a unit of time $\tau = \sigma\sqrt{m/\epsilon}$, with m being the mass of the monomers. Our systems consist of $N = 2.56 \times 10^5$ LJ particles randomly distributed within a cubic box at an initial monomer number density $\rho_m = 0.85\sigma^{-3}$. The equations of motion are integrated using the velocity Verlet algorithm, with a time step 0.005τ and the temperature set to $T = 1\epsilon/k_B$, thus representing a gel phase. The temperature is imposed using a Langevin thermostat with a damping coefficient of $\gamma = 1\tau^{-1}$. The initial LJ system is equilibrated for 10^6 steps. For the chain connectivity, we have used two different bond types, namely the finitely extensible nonlinear elastic (FENE) and the harmonic potentials.

1. FENE bond

A bond between two monomers is defined by the combination of repulsive 6-12 LJ potential,

$$u_{\text{bonded}}(r) = 4\epsilon_b\left[\left(\frac{\sigma_b}{r}\right)^{12} - \left(\frac{\sigma_b}{r}\right)^{6} + \frac{1}{4}\right] \quad \text{for } r < 2^{1/6}\sigma_b, \tag{2}$$

and the finite extensible nonlinear elastic (FENE) potential [31],

$$u_{\text{FENE}}(r) = -\frac{1}{2}kR_\circ^2 \ln\left[1 - \left(\frac{r}{R_\circ}\right)^2\right]. \tag{3}$$

Here, ϵ_b and σ_b are the LJ interaction energy and the LJ interaction length between bonded monomers, respectively. While the default FENE bond parameters, $k = 30\epsilon/\sigma^2$ and $R_\circ = 1.5\sigma$, give a typical bond length of $\ell_b \simeq 0.97\sigma$ [31], we have also parameterized the FENE interaction for different ℓ_b. The details of the parameters are listed in Table I. These parameters ensure that the FENE bond stiffness remains reasonably invariant with the changing ℓ_b. Here we note that, in this generic model, one bead corresponds to a rather large number of atomistic monomers [13]. Therefore, we will use this bond potential to mimic a crosslinker similar to the polyetheramine cured epoxy network [32] and rather fluffy monomer with phenylenediamines crosslinkers [26].

2. Harmonic bond

In most commodity polymers, such as polystyrene (PS), polyethylene (PE), poly(methyl methacrylate) (PMMA), poly(N-isopropyl acrylaime) (PNIPAm), poly(acrylic acid) (PAA), and poly(acrylamide) (PAM), the backbone connectivity is dictated by the carbon-carbon covalent bond [18]. For a polycarbonate chain, the chain connectivity is dictated by the phenol rings [33]. Both these bonds are significantly stiffer than most crosslinkers used to synthesize HCP [26,32]. Therefore, to mimic the stiff bonds, we have used the harmonic potential,

$$u_{\text{harmonic}}(r) = \frac{\epsilon}{2s^2}(r - \ell_b)^2, \tag{4}$$

with s being the standard deviation of the bond length fluctuation [33]. For this purpose, we have taken $s = 0.0126\sigma$, representing the linkages in polycarbonate [34], for $\ell_b = 0.90\sigma$, 0.97σ, 1.05σ, and 1.10σ. As noted earlier [34], we also wish to highlight that the fluctuation of the FENE bond is

TABLE I. Parameters of FENE potential. Here, ℓ_b, ϵ_b, and σ_b are the bond length, LJ interaction energy, and LJ interaction length, respectively. The interaction cutoff is chosen as $2^{1/6}\sigma_b$. The FENE bond stiffness k and length scale $R_\circ$ are also listed. Here, the parameters in the second row are the default Kremer-Grest model [31].

ℓ_b [σ]	ϵ_b [ϵ]	σ_b [σ]	k [ϵ/σ^2]	$R_\circ$ [σ]
0.87	1.0	0.9	37.0	1.35
0.97 [31]	1.0	1.0	30.0	1.50
1.07	1.0	1.1	24.5	1.65

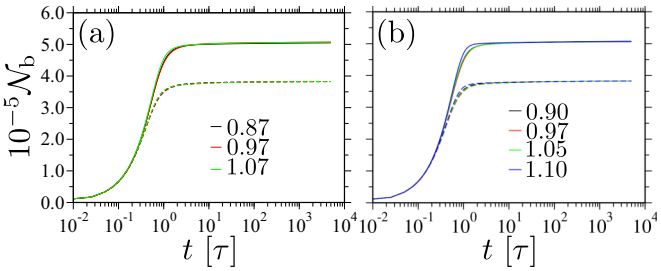

FIG. 1. The formation of the total number of bonds $\mathcal{N}_b$ with time t for different bond lengths ℓ_b. The data is shown for $n = 3$ trifunctional (dashed lines) and $n = 4$ tetrafunctional (solid lines) monomers. Parts (a) and (b) show the data for the FENE and the harmonic bonds, respectively.

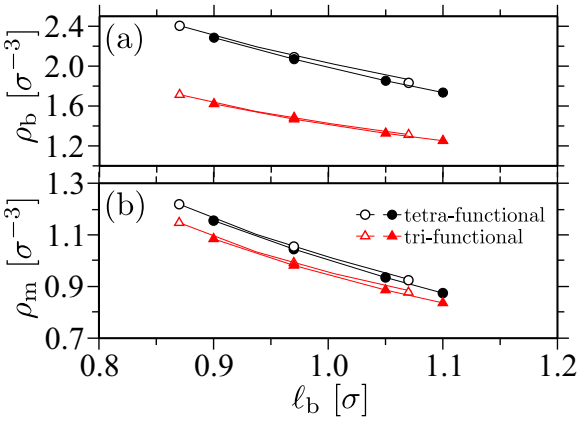

FIG. 2. Number density of bonds ρ_b (a) and monomers ρ_m (b) as a function of bond length ℓ_b. The data is shown for the systems after the isobaric equilibration. Open and solid symbols are for the FENE and the harmonic bonds, respectively. The lines are drawn to guide the eye.

about 3.4% at $T = 1\epsilon/k_B$, while this is only about 1% for the harmonic bond with $s = 0.0126\sigma$.

B. Thermal transport calculations

The thermal transport coefficient κ is calculated using the Kubo-Green method [35] implementation in LAMMPS [36]. The equations of motion are integrated in the microcanonical ensemble. The heat flux autocorrelation function $C(t) = \langle \mathbf{J}(t) \cdot \mathbf{J}(0) \rangle$ is obtained by sampling the heat flux vector $\mathbf{J}(t)$. The typical $C(t)$ data is shown in the Supplemental Material (Fig. S1) [37]. Here we choose a sampling period of 0.005τ to determine the correlation function within a timeframe of $0 \leqslant t \leqslant 50\tau$, which is one order of magnitude larger than the typical decorrelation time, see Fig. S1 [37]. During a total simulation time of $5 \times 10^4\tau$, we accumulate correlation data and compute a running average of $C(t)$. Finally, κ values are calculated by taking the plateau of the Green-Kubo integral,

$$\kappa = \frac{v}{3k_B T^2} \int_0^{\mathcal{T}} C(t)\mathrm{d}t, \tag{5}$$

where v is the system volume. Ideally the sampling time is $\mathcal{T} \to \infty$. Here, however, we calculate κ by taking an average between $30\tau \leqslant \mathcal{T} \leqslant 50\tau$ from the plateau of the cumulative integral in Eq. (5).

III. RESULTS AND DISCUSSIONS

A. Sample cure

The bonds are formed during a network curing stage using a similar protocol to one used earlier [14]. Within this protocol, starting from a LJ melt at $T = 1\epsilon/k_B$, bonds are randomly formed between a pair of particles when: 1) two particles are closer than $1.1\ell_b$ distance, 2) they have not formed the maximum number of allowed bonds n, and 3) a random number between zero and one is less than the bond forming probability of 0.05. Unless stated otherwise, the network curing is performed for 10^6 time steps (or equivalent of $t_{cure} = 5 \times 10^3\tau$) under the canonical simulation.

Figure 1 shows the formation of the total number of bonds $\mathcal{N}_b$ during the curing stage for different ℓ_b and n for both bond types. It can be seen that $\mathcal{N}_b$ values reach a plateau maximum around $t \simeq 10^2\tau$. We have also calculated the percentage of cure $\mathcal{C}$ after t_{cure}, see Fig. S2 [37]. It can be appreciated that all systems reach over 98.5% cure. Furthermore, $\mathcal{C}$ increases with ℓ_b by a factor of less than 1%. This slight increase in $\mathcal{C}$ is due to the pure geometric arrangements where a longer ℓ_b leads to a larger number of nearest neighbors, thus on average forming a larger number of bonds. Moreover, we find that the number densities of bonds ρ_b [see Fig. 2(a)] and monomers ρ_m [see Fig. 2(b)] decrease by 30-35% with increasing ℓ_b. We will come back to this density effect at a later stage of this article.

Another interesting feature of the network microstructure is the spontaneous formation of rather large voids immediately after the cure, see Figs. 3(a)–(d). The void formation in these systems is not surprising given that the two adjacent monomers can form all n bonds within a small solid angle pointing away from each other, while these two native monomers may or may not form bonds within themselves [14]. Furthermore, these void structures are dictated by the system thermodynamics- where, starting from a homogeneous monomeric mixture at a given ρ_m, the formation of a void with a particular size is dictated by the competition between the entropy penalty and the surface energy reduction. In this context, it has been previously shown these network microstructural features can lead to the interesting mechanical response of the HCP networks [12,32].

The void sizes become larger with decreasing ℓ_b [see the comparison between Figs. 3(a) and 3(c)] and n [see the comparison between Figs. 3(b) and 3(d)]. We have also calculated the void sizes in these systems using a protocol proposed earlier [14]. In this protocol, a simulation domain is divided into cubic voxels with 1σ box lengths. A voxel is considered to be a void if a particle is not within a distance 0.5σ from the voxel boundary. For $\ell_b = 0.90\sigma$, we find that the largest void is about $10 - 15\sigma^3$ for $n = 4$ and $\sim 60\sigma^3$ for $n = 3$. Moreover, for $\ell_b \geqslant 1.05\sigma$ voids are not present predominantly because of the homogeneous bond formation above a critical bond length. We also wish to note that the fractions of the total void volume v_{void} are on average smaller for the harmonic bonds in comparison to the FENE bonds, see Fig. 3(e). This observation is also not surprising given that, in our model,

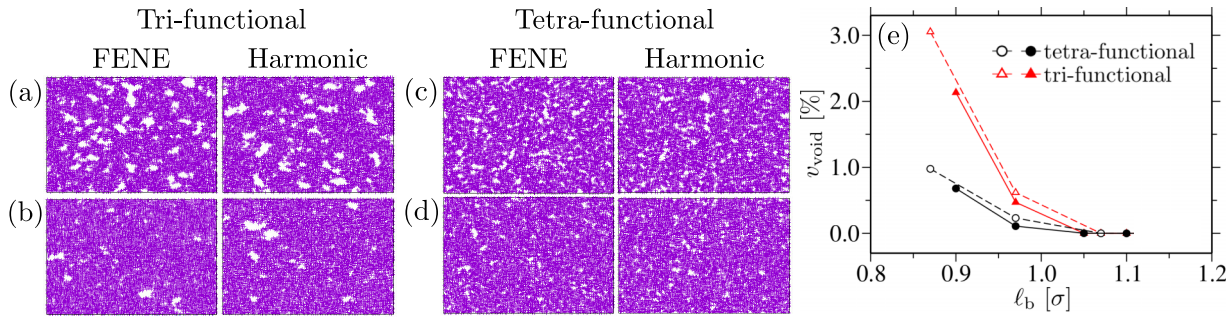

FIG. 3. (a)–(d) show the simulation snapshots of a 2σ thick layer along the z direction after the network cure in the canonical ensemble. The lateral dimensions of the snapshots are 67.03σ. Snapshots are shown for different bond lengths ℓ_b and functionalities n, as mentioned in the figure headings. (a) and (c) are for $\ell_b = 0.90\sigma$, and (b) and (d) are for $\ell_b = 0.97\sigma$. (e) shows the fraction of the void volume v_{void} as a function of ℓ_b. The open and the solid symbols are for the FENE and the harmonic bonds, respectively. The lines are drawn to guide the eye.

by construction the harmonic bonds are stiffer than the FENE bonds.

After the curing procedure, the systems are subsequently equilibrated in the isobaric ensemble at zero pressure. During this process the voids can collapse, forming several protovoids (void centers) within the sample [14]. The detailed structures are shown in the Supplemental Material (Section S2) and Figs. S3–S6 [37].

To summarize the network cure procedure, we find a few key features:

(i) The percentage of network cure $\mathcal{C}$ increases by $\simeq$1% with the bond length ℓ_b.

(ii) The number density of bonds ρ_b and monomers ρ_m decreases by $\simeq 30-35\%$ with ℓ_b, giving free volume and dilution of bonds.

(iii) The fraction of the total void volume v_{void} decreases with ℓ_b, reaching a vanishing value for $\ell_b \gtrsim 1.05\sigma$.

(iv) For $\ell_b > 1.05$, the bond formation in a network is rather homogeneous.

We will now show how the delicate balance between $\mathcal{C}$, ρ_b, v_{void}, and the bond stiffness can act as a guiding principle for κ tunability in crosslinked networks. Note, for the calculations of κ in each system, we have used six independent network configurations separately cured to obtain their respective microstructures.

B. Thermal conductivity

We will now discuss the most important results of this manuscript, namely the variation of κ with different system parameters, see Fig. 4.

It can be seen for the linear chains that κ remains invariant for both bonds, see the green □ and the blue ◇ data points in Fig. 4. Note that the nonbonded interactions are identical in these two model melts. Ideally, the stiffer bonds can lead to higher κ, i.e., the heat transfer between two bonded monomers can increase with bond stiffness. Moreover, the typical length scale over which this increased κ can be observed (or the mean free path of the heat flow) is only about 2–3 monomer units (i.e., the typical segment length) [38]. Over the full chain backbone, however, κ can be significantly reduced. This is because a chain conformation in a melt is a random walk [31,39], thus forming several bends along the chain contour. Here, each bend acts as a scattering center for the heat flow. The higher the number of bends along the backbone, the lower the κ [40,41]. It is also important to note that the typical end-to-end distance R_{ee} of a chain with $N_\ell = 50$ in a melt is $R_{ee} \simeq 10\sigma$, which is only about 15% of the box length $L \simeq 66.2\sigma$. Therefore, for a linear polymer melt the major dominating effect on κ is due to the vdW-based nonbonded interactions, while bond stiffness plays a lesser contribution to κ. For example, in the case of the standard polymers, such as PMMA, PS, and PE, where vdW interactions are dominant, $0.1 \leqslant \kappa \leqslant 0.2$ W/Km [17,20]. Moreover, in the case of the hydrogen bond contacts, $\kappa \to 0.4$ W/Km [17,18], such as PAM, PAA, and PNIPAM. We also wish to highlight that all these vdW or the hydrogen bond-based systems have a very similar covalently bonded carbon-carbon backbone.

With increasing n, where the bonded interaction forming the network has the dominant contribution, the difference in κ becomes more prominent between the harmonic and the

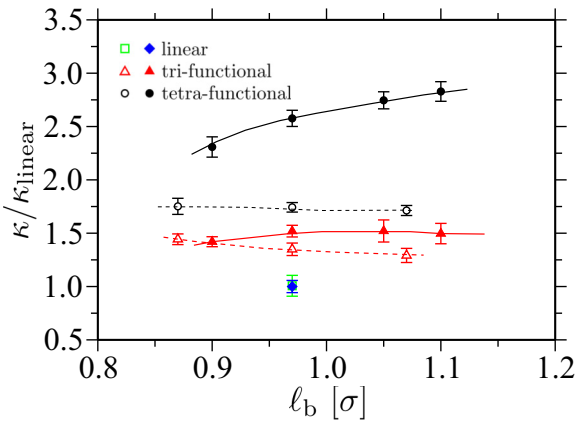

FIG. 4. The normalized thermal transport coefficient κ/κ_{linear} as a function of the bond length ℓ_b. The data is shown for different network functionality n and for both bonds. The data is normalized with respect to the linear chain connected by the harmonic springs giving $\kappa_{linear} = 5.4 \pm 0.3\ k_B/\tau\sigma$. Here the linear chain lengths are chosen as $N_\ell = 50$. The open and the solid symbols are for the FENE and the harmonic bonds, respectively. The lines are drawn to guide the eye. The error bars are the standard deviations calculated from the κ values obtained from the six independent simulation runs.

FENE bonds, see the comparison between the black solid and open ○ data sets in Fig. 4. See also the comparison between the red solid and open △ data sets in Fig. 4.

A closer look at the data sets corresponding to the FENE bond further reveal that κ remains almost invariant with ℓ_b, see the data sets corresponding to the open ○ and △ in Fig. 4. This is predominantly due to the fact that the competing effects, i.e., the reduction in ρ_b with ℓ_b that reduces κ (see part a of Fig. 2) and the decrease in v_{void} with ℓ_b that increases κ [see Fig. 3(e)], cancel each other. The latter also induces a more homogeneous bond formation within the network.

It is also important to discuss how v_{void} influences the κ behavior. In these network structures, the protovoids usually act as the scattering centers for the heat flow, where the most preferred heat propagation pathway is the bonded monomers along the circumference around the protovoids. The larger the fraction of v_{void}, the larger the hindrance to the heat flow, and thus the lower the value of κ.

In the case of the harmonic bonds, both trifunctional and tetrafunctional networks show a 5–10% increase in κ with ℓ_b, see the data sets corresponding to the solid ○ and △ in Fig. 4. It is worth noting that a stiffer bond strength plays an additional positive contribution to the κ behavior. To further illustrate that the bond stiffness is the key factor for the above mentioned increase in κ, we have performed one more set of simulations where $\epsilon/2s^2$ is reduced by a factor of 6. Here, $\kappa/\kappa_{linear} \simeq 1.81$ for all four ℓ_b, which is comparable to the FENE bond data for $n = 4$, see the open black ○ data set in Fig. 4.

C. Thermal conductivity, heat capacity and sound wave velocity

So far we have discussed the behavior of κ with respect to the network microstructure and bond stiffness. Moreover, it has been shown that κ is related to the velocity of sound wave v and the volumetric specific heat c_v [15]. Therefore, in this section we will discuss the possible influence of the network microstructure on v and its correlation with κ. For this purpose, we have used the simplified estimate $v = \sqrt{K/\rho_m}$, where K is the bulk modulus. Here, K is calculated using the fluctuation of volume V in the isobaric ensemble following the relation,

$$K = k_B T \frac{\langle V \rangle}{\langle V^2 \rangle - \langle V \rangle^2}. \quad (6)$$

The volume fluctuation is sampled over a time $5 \times 10^4 \tau$ with a time output interval of 0.5τ. Since we are performing classical simulations, we estimate c_v using the Dulong-Petit limit $3\rho_m k_B$. Note that while we report c_v using a simple estimate, we have also calculated c_v using dE/dT for a couple of configurations that show only about 2% variation from $3\rho_m k_B$ values (data not shown).

In Fig. 5 we show the variation in κ with c_v and v. It can be seen that, while these data sets overall show a rather nontrivial functional dependence (as also experimentally reported for HCP [26]), κ values show on average a consistent increase with increasing v for the the individual sets. More specifically, going from the linear chains to a trifunctional system and then to a tetrafunctional system, we observe $\kappa \propto v$, see Fig. 5(b). However, within a given system with varying ℓ_b,

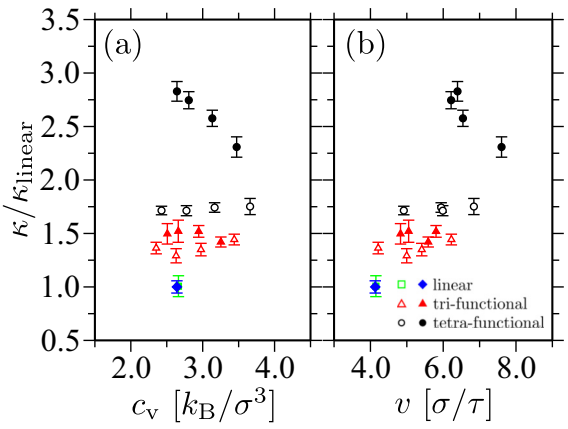

FIG. 5. The normalized thermal transport coefficient κ/κ_{linear} as a function of the volumetric specific heat c_v (a) and the sound wave velocity v (b). The data is shown for different functionality n, bond length ℓ_b, and for both bonds. The data is normalized with respect to the linear chain connected by the harmonic springs, giving $\kappa_{linear} = 5.4 \pm 0.3\ k_B/\tau\sigma$. Here, the linear chain lengths are chosen as $N_\ell = 50$. The open and the solid symbols are for the FENE and the harmonic bonds, respectively. The error bars are the standard deviations calculated from the κ values obtained from the six independent simulation runs.

several competing factors contribute to the nontrivial functional dependence, i.e., the delicate balance between ρ_b, ρ_m, v_{void}, and bond stiffness dictate the κ behavior. For example, when $n = 4$ (or the tetrafunctional HCP) and the bonds are harmonic, κ increases with decreasing v. This is an effect of decreasing ρ_m and homogeneous bond formation in the networks that induces a rather void-free sample, see the black solid ○ data set in Fig. 5.

D. Possible comparison with the realistic systems

The generic simulation data presented in this study highlights the importance of bond engineering and network microstructure on the heat management in HCP. However, the major question still remains if the results presented here can be compared with the experimentally relevant realistic systems. In this context, it is important to mention that the increased bonding in HCP ideally provides a suitable pathway for the faster heat flow. This would therefore mean an increase in κ by a large fraction compared to the linear polymeric materials. Here, however, we only find an increase in κ of about a factor of 1.5 for the trifunctional and 1.7–2.7 for the tetrafunctional HCP, see Fig. 4. Now, considering the standard linear polymeric materials such as PMMA or PS that has $\kappa \simeq 0.1 - 0.2$ W/Km [17,18,20] and the experimental data for HCP in Ref. [26], we find that $\kappa/\kappa_{linear} \sim 1.1 - 2.0$ for different crosslinkers. This range is consistent with all the data sets presented in Fig. 4 except for the tetrafunctional HCP with the harmonic bonds, see the black solid ○ data set in Fig. 4. Furthermore, the most common HCP are synthesized either with fluffy bonds and monomers [32] and/or with fluffy monomers and stiff crosslinkers [26]. In our model, the FENE bond type mimics these conditions closely and thus shows

reasonably good agreement with the experimental observations [26].

In some cases, crosslinking can also decrease κ compared to the linear chains, such as the crosslinked PAA system compared to the linear PAA [17]. Here, however, the length of the crosslinkers are rather large and thus can have large entropic fluctuations. Recent all-atom simulation results have shown that the length of the crosslinkers significantly contribute to the observed trends in κ behavior [38]. For example, when a long PAA chain system is blended with PAM trimers that can form hydrogen-bonded crosslinking between two PAA monomers of the different chains, κ can slight enhance in comparison to a pure PAA [38]. These trends, observed in experimental and all-atom simulation data, that κ is closely impacted by the length of the crosslinkers are also consistent with the generic simulations [27].

Another possible route for the synthesis of HCP might be to use the linear polymer chains, either homopolymer or copolymer, and crosslinking them using the stiff N,N'-methylenebis(acrylamide) (BIS) [42]. In this system, it has been shown that a crosslinked microgel of P(NIPAM-co-AA) with only about 5% BIS can significantly increase its elastic modulus [43]. It would therefore be interesting to experimentally investigate a system with a large degree of BIS crosslinking that may give a further increase in κ for network structures.

Lastly, we would also like to comment on the tunability in κ. For example, while it is always desirable to increase κ of materials for their possible use under the high temperature conditions [5,7], crosslinked thermoelectric materials [9,10] require an ultralow κ for better device performance. Here, the fraction of engineered protovoids within the cured network may provide an additional pathway for the tunability in κ. In this context, as discussed in the Sec. III A, the generic features of the network microstructure naturally emerge because of the thermodynamic reasons. In experiments, the engineered protovoids with different fractions can be incorporated by including a nonreactive solvent (such as tetrahydrofuran or dichloromethane) during the network curing stage. Inclusion of a nonreactive solvent facilitates the bond formation around a solvent bubble [32]. Here, the change in nonreactive solvent content is then expected to change the protovoids fractions within a sample, and thus κ. The encapsulated solvents can then be extracted during a post-cure procedure following an earlier treatment [32].

IV. CONCLUSIONS

We have performed large scale molecular dynamics simulations of two different generic polymer models to study the thermal transport in the highly crosslinked polymers (HCP). We emphasized the importance of engineered crosslinking bond types that in turn gives an additional pathway to introduce a tunability in the thermal transport coefficient κ of HCP. These results show that the spontaneous formation of molecular scale voids/protovoids during the curing procedure, the bond density, the bond length, and the bond stiffness, together with the delicate balance between these competing effects, ultimately dictate the behavior of κ. While our simulation data sets present a generic physical picture and the importance of the underlying network microstructure, we also present a comparative discussion in the context of the different experimentally relevant systems. Based on our analysis, we also sketch a set of directions that may be useful for the design of future materials for their possible uses in advanced functional applications.

ACKNOWLEDGMENTS

D.M. thanks the Canada First Research Excellence Fund (CFREF) for financial support. Simulations are performed at the Advanced Research Computing Sockeye facility of the University of British Columbia, the Compute Canada facility, and the LISA cluster at the Quantum Matter Institute. M.K.S. thanks the IIT Kanpur initiation grant for providing financial support and the computational facilities to create and test the input scripts and initial trajectories for simulations.

[1] M. A. Cohen-Stuart, W. T. S. Huck, J. Genzer, M. Müller, C. Ober, M. Stamm, G. B. Sukhorukov, I. Szleifer, V. V. Tsukruk, M. Urban, F. Winnik, S. Zauscher, I. Luzinov, and S. Minko, Nat. Mater. **9**, 101 (2010).

[2] D. Mukherji, C. M. Marques, and K. Kremer, Annu. Rev. Condens. Matter Phys. **11**, 271 (2020).

[3] A. Henry, Ann. Rev. Heat Transfer **17**, 485 (2014).

[4] N. Mehra, L. Mu, T. Ji, X. Yang, J. Kong, J. Gu, and J. Zhua, Appl. Mater. Today **12**, 92 (2018).

[5] G. Kim, D. Lee, A. Shanker, L. Shao, M. S. Kwon, D. Gidley, J. Kim, and K. P. Pipe, Nat. Mater. **14**, 295 (2015).

[6] N. Kim, B. Domercq, S. Yoo, A. Christensen, B. Kippelen, and S. Graham, Appl. Phys. Lett. **87**, 241908 (2005).

[7] M. K. Smith, V. Singh, K. Kalaitzidou, and B. A. Cola, ACS Appl. Mater. Int. **8**, 14788 (2016).

[8] W. Shi, Z. Shuai, and D. Wang, Adv. Funct. Mater. **27**, 1702847 (2017).

[9] T. Liu, A. Shinohara, G. Tan, C. Pan, and L. Wang, Macromol. Mater. Eng. **304**, 1800730 (2019).

[10] J. Park, Y. Lee, M. Kim, Y. Kim, A. Tripathi, Y.-W. Kwon, J. Kwak, and H. Y. Woo, ACS Appl. Mater. Interfaces **12**, 1110 (2020).

[11] I. M. McAninch, G. R. Palmese, J. L. Lenhart, and J. J. L. Scala, Appl. Polym. Sci. **130**, 1621 (2013).

[12] R. M. Elder, D. B. Knorr, J. W. Andzelm, J. L. Lenhart, and T. W. Sirk, Soft Matter **12**, 4418 (2016).

[13] M. J. Stevens, Macromolecules **34**, 2710 (2001).

[14] D. Mukherji and C. F. Abrams, Phys. Rev. E **78**, 050801(R) (2008).

[15] D. G. Cahill, S. K. Watson, and R. O. Pohl, Phys. Rev. B **46**, 6131 (1992).

[16] J. L. Braun, C. M. Rost, M. Lim, A. Giri, D. H. Olson, G. N. Kotsonis, G. Stan, D. W. Brenner, J.-P. Maria, and P. E. Hopkins, Adv. Mater. **30**, 1805004 (2018).

[17] X. Xie, D. Li, T. Tsai, J. Liu, P. V. Braun, and D. G. Cahill, Macromolecules **49**, 972 (2016).
[18] C. Ruscher, J. Rottler, C. E. Boott, M. J. MacLachlan, and D. Mukherji, Phys. Rev. Mater. **3**, 125604 (2019).
[19] A. Henry and G. Chen, Phys. Rev. Lett. **101**, 235502 (2008).
[20] S. Shen, A. Henry, J. Tong, R. Zheng, and G. Chen, Nat. Nanotech. **5**, 251 (2010).
[21] J. Liu and R. Yang, Phys. Rev. B **86**, 104307 (2012).
[22] T. Zhang and T. Luo, ACS Nano **7**, 7592 (2013).
[23] G. P. Desiraju, Acc. Chem. Res. **35**, 565 (2002).
[24] B. Crist and P. G. Herena, J. Polym. Sci. Part B: Polym. Phys. **34**, 449 (1996).
[25] V. Varsney, S. S. Patnaik, A. K. Roy, and B. L. Farmer, Polymer **50**, 3378 (2009).
[26] E. Jensen, C. Shen, K. Yang, C. M. Evans, and D. G. Cahill, ACS Appl. Polym. Mater. **3**, 259 (2021).
[27] R. Huo, Z. Zhang, N. Athir, Y. Fan, J. Liu, and L. Shi, Phys. Chem. Chem. Phys. **22**, 19735 (2020).
[28] A. Aramoon, T. D. Breitzman, C. Woodward, and J. A. El-Awady, J. Phys. Chem. B **120**, 9495 (2016).
[29] A. K. Pervaje, J. C. Tilly, A. T. Detwiler, R. J. Spontak, S. A. Khan, and E. E. Santiso, Macromolecules **53**, 2310 (2020).
[30] P. V. Komarov, C. Yu-Tsung, C. Shih-Ming, P. G. Khalatur, and P. Reineker, Macromolecules **40**, 8104 (2007).
[31] K. Kremer and G. S. Grest, J. Chem. Phys. **92**, 5057 (1990).
[32] M. Sharifi, C. W. Jang, C. F. Abrams, and G. R. Palmese, J. Mater. Chem. A **2**, 16071 (2014).
[33] W. Tschöp, K. Kremer, J. Batoulis, T. Bürger, and O. Hahn, Acta Polym. **49**, 61 (1998).
[34] C. F. Abrams and K. Kremer, J. Chem. Phys. **115**, 2776 (2001).
[35] R. Zwanzig, Annu. Rev. Phys. Chem. **16**, 67 (1965).
[36] S. Plimpton, J. Comput. Phys. **117**, 1 (1995).
[37] See Supplemental Material at http://link.aps.org/supplemental/10.1103/PhysRevMaterials.5.025602 for data of the heat-flux autocorrelation function, the simulation snapshots of the HCP networks, and the effect of initial density on the thermal transport coefficient of HCP.
[38] D. Bruns, T. E. de Oliveira, J. Rottler, and D. Mukherji, Macromolecules **52**, 5510 (2019).
[39] M. Doi, *Soft Matter Physics* (Oxford University Press, Oxford, 2013).
[40] X. Duan, Z. Li, J. Liu, G. Chen, and X. Li, J. Appl. Phys. **125**, 164303 (2019).
[41] A. Bhardwaj, A. S. Phani, A. Nojeh, and D. Mukherji, ACS Nano **15**, 1826 (2021).
[42] S. Backes, P. Krause, W. Tabaka, M. U. Witt, D. Mukherji, K. Kremer, and R. von Klitzing, ACS Macro Lett. **6**, 1042 (2017).
[43] S. Backes, P. Krause, W. Tabaka, M. U. Witt, and R. von Klitzing, Langmuir **33**, 14269 (2017).